From manned to unmanned aircraft: Adapting airborne particle size mapping methodologies to the characteristics of sUAS and SfM

Woodget, A.S., Fyffe, C. and Carbonneau, P.E.

Abstract

Subaerial particle size data holds a wealth of valuable information for fluvial, coastal, glacial and other sedimentological applications. Recently, we have gained the opportunity to map and quantify particle sizes at the mesoscale using data derived from small unmanned aerial system (sUAS) imagery processed using structure from motion (SfM) photogrammetry. These sUAS-SfM approaches have been based typically on calibrating orthoimage texture or point cloud roughness with particle size. Variable levels of success are reported and a single, robust method capable of producing consistently accurate and precise results in a range of settings has remained elusive. In this paper, we develop an original method for particle size mapping with the specific constraints of sUAS and SfM in mind. This method uses the texture of single sUAS images, rather than orthoimages, calibrated with particle sizes normalised by individual image scale. We compare results against existing orthoimage texture and roughness approaches, and provide the first quantitative investigation into the implications of the use of sUAS camera gimbals. Our results indicate that our novel single image method delivers the optimal particle size mapping performance for our study site, outperforming both other methods and delivering residual mean errors of 0.02mm (accuracy), standard deviation of residual errors of 6.90mm (precision) and maximum residual errors of 16.50mm. Accuracy values are more than two orders of magnitude worse when a camera gimbal is not used, thereby demonstrating the critical importance of mechanical image stabilisation for particle size mapping using measures of image texture.

Introduction

The quantification of subaerial particle sizes is of value in a range of environmental scenarios. In river science, for instance, we rely on mapping particle size distributions for assessing habitat quality and diversity, for modelling flow hydraulics and determining the impact of fluvial transport on engineering structures, flood protection measures and restoration works. Here, we use the term ‘particle size’ interchangeably with ‘grain size’ to refer to material typically within the gravel size classification and larger (Wentworth, 1922). Traditional methods of characterising grain size distributions include quantitative sampling, such as laboratory based sieving or the measurement of in-situ grains at set intervals along transects, as well as qualitative classification schemes such as the Wentworth Scale (Wentworth, 1922; Wolman, 1954; Hey and Thorne, 1983; Church et al., 1987; Rice and Church, 1996). In recent decades, remote sensing approaches have provided alternative techniques that are typically faster, less labour intensive and less affected by bias than traditional manual measurements (Leopold, 1970; Church et al., 1987; Verdú et al., 2005). Readers are referred to Woodget and Austrums (2017) for an overview of the key remote sensing methods used for grain size quantification to date. These methods can be broadly categorised into two main schools of thought, where the focus is typically on either;

(1) The use of high resolution remotely sensed data to delineate individual grains, or;

(2) The development of a statistical relationship between grain size and remotely sensed data properties.

The former, commonly referred to as ‘photo-sieving’, has been dominated by the use of close range, high-resolution photography, often collected by hand or from tripods

and gantries set up over the material of interest (Adams, 1979; Ibbeken and Schleyer, 1986; Butler et al., 2001; Sime and Ferguson, 2003). Automated software packages (e.g. Sedimetrics, Basegrain) have been developed to measure individual grains with high levels of accuracy (Graham et al., 2005a; Graham et al., 2005b; Detert and Wietbrecht, 2012).

The second category comprises a variety of methods used to establish a correlation with measured grain sizes, including;

(a) Textural analysis of imagery collected from manned aircraft (Carbonneau et al., 2004; Carbonneau, 2005; Carbonneau et al., 2005; Verdú et al., 2005).

(b) Analysis of the roughness of point cloud data obtained from terrestrial laser scanners (TLS) (McEwan et al., 2000; Entwistle and Fuller, 2009; Heritage and Milan, 2009; Hodge et al., 2009; Brasington et al., 2012; Milan and Heritage, 2012; Rychov et al., 2012; Baewert et al., 2014).

(c) Analysis of the spectral or frequency content of imagery acquired at close range (Rubin, 2004; Buscombe, 2008; Buscombe and Masselink, 2009; Buscombe et al., 2010; Buscombe and Rubin, 2012; Buscombe, 2013).

These methods have been established in a variety of sedimentological settings, but here we focus on their application to river systems in particular. Whilst approach (a) is used at the macroscale (i.e. over many kilometres of channel length at metre spatial resolution), and method (c) at the patch scale (i.e. over about a square metre, with millimetre spatial resolution), few methods are yet capable of surveying grain size at the mesohabitat scale (i.e. channel lengths of 50-500m with centimetre spatial resolution) without the significant expense of purchasing a laser scanner

under method (b). Critically however, the mesoscale is the scale most relevant for fluvial ecosystems and the health and survival of their inhabitant biota (Newson and Newson, 2000).

Very recently, the development of small unmanned aerial systems (sUAS) and structure from motion digital photogrammetry (SfM) (e.g. Westoby et al., 2012; Fonstad et al., 2013) has provided a new remote sensing based approach for fluvial surveying, which has shown great potential for application at the mesoscale (Woodget et al., 2017). Outputs from sUAS-SfM typically comprise an orthoimage, a digital elevation model (DEM) and a dense point cloud, similar to the point clouds obtained using TLS. Data acquired using a sUAS-SfM approach has been tested using both the image textural analysis methods of group (a) and the point cloud roughness methods of group (b).

The work of de Haas et al., (2014) found that images acquired from sUAS, which are more unstable than manned aircraft, suffer from blurring which precludes a strong predictive relationship between image texture and grain size. In contrast, Tamminga et al., (2015) found strong calibration relationships ($R^2 = 0.82$), but these could not be replicated by the more recent work of Woodget and Austrums (2017), where the best calibration relationships reached an R^2 of just 0.48. Woodget and Austrums (2017) also report weak validation relationships, as indicated by a slope of 0.44 for the observed versus predicted grain size relationship. They suggest that these poor results, as well as those of de Haas et al., (2014), relate to the use of an inadequate camera gimbal that introduces additional blur to the sUAS imagery. The set-up used by Tamminga et al., (2015) featured a more advanced gimbal, isolating the camera from platform vibrations and permitting the collection of higher quality images. In addition, earlier work on the texture method, by Carbonneau et al., 2004 and Verdú

et al., 2005, found that the process of orthorectification introduces further visual distortions that then negatively affected grain size predictions. It is likely then, that the SfM orthorectification process may be partly responsible for limiting the strength of results obtained from sUAS platforms.

Point cloud roughness approaches using sUAS-SfM data have also been demonstrated recently, as pioneered by Woodget (2015) and subsequently applied by others (Vázquez-Tarrío et al., 2017; Woodget and Austrums, 2017). Inspired by methods used with TLS data (e.g. Brasington et al., 2012), these papers sought to develop a predictive calibration between the roughness of dense point clouds (i.e. fine scale variation in elevation of the points), obtained using the SfM process, with grain size data. To date, more consistent results have been obtained using this method than by using image textural approaches. Vázquez-Tarrío et al., (2017) report high R^2 calibration values (R^2 = 0.89), as do Woodget and Austrums (2017) (R^2 = 0.80) and others (M. Detert, *pers. comm*). Validation results are also promising, and with mean errors of <1mm and standard deviation of errors of <2cm (Woodget and Austrums, 2017).

Despite the encouraging outcomes of some of these initial studies however, quantitative investigations aimed at explaining the discrepancies in results between different papers is lacking. Furthermore, we are largely reliant on methods which have been developed with manned aircraft or terrestrial laser scanners in mind, which may not be wholly suitable when applied to sUAS-SfM data. Further investigation is therefore necessary if we are to develop a consistent and reliable method of determining grain size distributions at the critical mesoscale, both in fluvial settings and beyond. Therefore, within this paper, our main aim is to present a comprehensive approach to particle sizing from sUAS platforms that relies on

methods designed with the specific characteristics of sUAS image acquisition and flight patterns in mind. We address the following objectives:

(1) To quantify the impact of camera gimbals (i.e. sUAS image blur) on the derived metrics of orthophoto image texture which are used to model grain sizes.

(2) To adapt image-based methods of grain size determination developed for manned aircraft to sUAS and compare performance to the derived metrics obtained under objective 1.

Site Details

We selected a c. 80m long fluvial gravel bar for this research, which is located along the right bank of the River Wear, near Willington, County Durham, UK. At this location, the River Wear is c. 20m wide, with a bed composed of imbricated gravels and cobbles. A pre-flight visit confirmed that this site was easily accessible and safe for sUAS flying.

Methods

sUAS surveys

We acquired image data in July 2016 during dry and bright weather conditions. To investigate the effects of sUAS image blur, we flew two different rotary-winged sUAS at the River Wear, with different camera gimbal set-ups. The first was a DJI Phantom 3 Pro (P3P) with an integrated camera held within a 3-axis brushless gimbal. The P3P camera has a resolution of 12Mp and a field of view (FOV) of 94°. The second was an older platform, a DJI F550, mounted with a Canon Powershot S100 camera

having a resolution of 12Mp and an FOV of 84°, which we strapped to the underside of the sUAS without the use of a gimbal. We used each sUAS to perform two surveys:

- Survey 1 comprised the collection of a series of images whilst hovering the sUAS above a set location on the gravel bar, to address objective (1).
- Survey 2 involved collecting imagery over the entire area of interest, to address objectives (1) and (2).

For survey 1, we flew each sUAS at an altitude of 20-30m to collect a series of RGB images of a set location on the gravel bar. For survey 2, we flew each sUAS at heights of c. 20m and 50m above ground level to collect RGB imagery of the whole site. Dual altitudes were used in accordance with the findings of Carbonneau and Dietrich (2017). This flight was easily controlled using the P3P since the flight controller app displays altitude in real time. For the F550, a best guess of the altitude was made by the pilot due to a lack of available flight information. We obtained imagery with a high level of overlap (c. 80%) and with a mix of nadir and convergent view angles, to facilitate camera self-calibration during the subsequent SfM processing. Figure 2 presents the resulting flying altitudes that were estimated *a posteriori* with the photogrammetry outputs described below. We note the much greater variability in flying altitudes for the F550 which reflects the manual nature of the F550 surveys. The gravel bar was systematically imaged with nadir imagery and convergent view imagery was added to support the nadir imagery. For the P3P, the off-nadir imagery was acquired with a simple change in the camera angle using the gimbal. For the F550 and the non-gimballed camera, we used a bespoke set-up to fix the camera at an angle. We acquired more than 100 images using each sUAS.

We distributed 10 ground control points (GCPs) prior to the sUAS surveys and positioned them carefully, based on prior experience, to ensure adequate representation of variations in topography within our site. We used a total station to survey the position of each GCP in a local co-ordinate system.

Ground truthing

To calibrate and validate the grain size determination models for objective (2), we established 30 ground truth plots along the gravel bar. Each plot was $1m^2$ in size and efforts were made to ensure within plot grain size was as uniform as possible, since plot uniformity is known to impact upon the strength of the grain size/roughness relationship (Pearson et al., 2017; Woodget and Austrums, 2017). We recorded the location of two opposing corners of each plot using a total station and acquired a scaled, close-range photograph of the plot using a handheld digital camera. Next, we georeferenced each photograph within a GIS environment based on the associated total station data.

Within the GIS environment, we selected a sample of grains for measurement by placing a regular 10 cm x 10 cm grid over each ground truth photograph (Figure 3). Those grains that fell beneath each grid node were measured for their A- and B-axes dimensions using the scaled and reference photograph of each plot (Figure 3). Some grains were unsuitable for measurement, including those that were obscured by other grains, those that were not fully visible within the photograph and those that were too small to measure at a scale of 1:1. We used these measurements to compute grain size statistics for each plot, including the mean, D_{50} and D_{84} of both the A- and B-axes.

Structure from motion photogrammetry

Prior to SfM processing, we conducted a subjective quality check on all Survey 2 images from both sUAS. We excluded images with notable blur or other visual artefacts from further processing. Whilst this was a subjective decision based on prior experience, subsequent results suggest that in future this could be established quantitatively using image entropy information. Sufficient redundancy within the surveys meant we would exclude images without compromising the subsequent processing chain. We imported a total of 70 P3P images and 79 F550 images from Survey 2 into Agisoft's PhotoScan Pro digital photogrammetry software. These image sets were processed separately to create an orthophoto (c. 1cm resolution) and a dense 3D point cloud for each sUAS set-up. We referenced all data to the local co-ordinate system by importing GCP locations and optimising the image alignments accordingly. Further information on the SfM-photogrammetry method can be found in recent papers by Fonstad et al., (2013), Smith et al., (2015) and Eltner et al., (2016).

Quantifying the impact of camera gimbals

To judge the quality of imagery collected by the two sUAS during Survey 1, we employed the 'Estimate image quality' tool within Agisoft's PhotoScan Pro software. This tool returns a value between 0 and 1, where higher values relate to higher quality images (Agisoft, *pers. comm.*). Using this information, we selected a set of 15 images for each sUAS survey over a range of image qualities, including the best and worst quality images. Whilst maintaining a range of image qualities, we also ensured that all images had a minimum image quality of 0.5, because lower quality images are not recommended for photogrammetric processing (Agisoft LLC, 2016). The

image quality of the F550 images ranged from 0.582 to 0.803, with the P3P image quality ranging from 0.828 to 0.834. It should be noted that the PhotoScan image quality does not specifically measure image blur, but instead provides a normalised measure of image quality, relating to the sharpest area of the image (Agisoft, *pers. comm.*). As a result and in order to better compare between images (and gimbal set-ups), for subsequent analysis we decided to use a measure of image entropy as indicative of the magnitude of image blur, since this would allow a more consistent and repeatable approach.

Entropy (E) is defined by Equation 1, which uses a grey level co-occurrence matrix (Haralick et al., 1973). This matrix (P) reports the probabilities of all pairwise (i, j) grey level combinations occurring within a neighbourhood of a specified size. We computed entropy for every image within each set using the *Entropyfilt* function in Matlab (Mathworks Inc.), with a neighbourhood size of 21 pixels on only the red band of the image (i.e. a greyscale image). High entropy values indicate large differences in the spectral values of neighbouring pixels. This suggests that the imagery is sharp and of high quality. In contrast, blurred imagery features small differences between nearby pixels and therefore lower entropy values.

$$E = -\sum_{i,j} P_{i,j} \left(\log 2 P_{i,j}\right)$$

Equation 1.

Next, we used the *OpenSURF* feature point matching function in Matlab (Kroon, 2010) to find the 30 best matched points between the image with the highest entropy (i.e. highest quality) and the remaining 14 images within each sUAS image set (using full colour images). We exported the coordinates of each of these matched points,

and at the location of each point, we extracted the entropy values for each pair of images within each set. This allowed us to compare the entropy for the same location between the highest quality image and each of the other images in the set. As a result, where values of entropy between the best image and the matched image are similar we would expect consistent image quality, and where they diverge we would expect inconsistent image quality, with the entropy values at each point relating to the level of blur.

Grain size mapping: Image-based approaches

We use both (a) orthomosaics and (b) single, non-mosaicked, images from both the F550 and the P3P drones:

(a) The Orthomosaic Approach

PhotoScan was used to produce orthomosaics with spatial resolutions of 11mm for the F550 and 9mm for the P3P. Verdú et al., (2005) suggest the use of image orthomosaics in grain size mapping because they have a constant scale. However, de Haas et al., (2014) found that image mosaics produced from non-gimballed sUAS images have considerable and spatially variable levels of image blur that can significantly affect grain-size mapping performance. Here, we aim to separate out the effect of camera gimbal from the possible noise induced by the orthomosaicking process. Additionally, it is now well established that texture-based grain size mapping approaches are sensitive to the kernel size used during the local texture mapping process (Carbonneau, 2005; Carbonneau et al., 2005a, Carbonneau et al., 2005b, Black et al., 2014). Therefore, here we use an iterative approach that scans through a range of kernel sizes in a Leave-One-Out Cross-Validation (LOOCV)

approach that simultaneously calibrates and validates the grain sizes against local values of textural entropy.

For the purpose of calibration, we introduce a key innovation to the grain size mapping process: dimensionless grain sizes. Co-occurrence based metrics, such as entropy, compare pixel brightness values for pairs of pixels separated by a fixed distance which is measured in image pixel units. In order to harmonise the units used in the grain size mapping algorithm, we normalise the grain sizes measured in the field by the spatial resolution of the image where they are captured. For the orthomosaic approach, this equates to using the unique spatial resolution of the orthomosaic (9mm for the P3P and 11mm for the F550).

The analysis begins by pre-calculating and storing textural entropy images obtained from a range of kernel sizes ranging from 5 to 101 pixels, in steps of 4 pixels, for each orthomosaic. Then, we take the D_{50} of the B-axis calculated for each ground truth plot. The LOOCV process starts by excluding the data from the first plot. For the remaining 29 plots, the D_{50} is normalised by the spatial resolution of the orthomosaic and the algorithm builds a table of normalised D_{50} vs. entropy values for the first kernel size. These values are regressed to determine a linear model which is then used to predict and store the value of the excluded plot. The LOOCV code loop then iterates and excludes the second of 30 plots and repeats the calibration for the first kernel size. Once all 30 plots have been excluded and the corresponding 32 predictions calculated, we iterate the kernel size, reset the LOOCV loop and repeat the entire process for kernel sizes ranging from 5 pixels to 101 pixels in

steps of 4 pixels. This algorithm is applied to the orthomosaics from both the F550 and P3P sUAS. The results are analysed by identifying the calibration with the strongest fit (via the adjusted R^2) and the corresponding quality of the predictions. Figure 4 shows a flowchart for this process.

(b) The Single Image Approach

Given the observations of de Haas et al., (2014), we now develop a method that obviates the orthomosaic by using a series of individual images which cover the study site. As noted by Verdú et al., (2005), in a critique of Carbonneau et al., (2004), one issue in using individual images is the possibility of variable scale, which weakens the cross-comparability of image textures calculated on image pixel units which have slightly different scales. We expect this effect to be even more significant for sUAS imagery since the lower flying heights and weaker altitude control will lead to greater variations in scale than those experienced with manned aircraft. In the case of the present data, the data in Figure 2 shows variability in the flying altitudes. Even for the automated flight of the P3P surveys, we find that the altitude of imagery collected at 20m AGL has a standard deviation of 0.53m. For the F550, standard deviation of the lower altitude flights was 3.44 m. Another related difficulty in working with single images is the need to establish a spatial reference system that can allow for a geospatial algorithm to retrieve ground truth values of grain size, referenced to map coordinates, and compare them to local texture values. We therefore begin by developing a semi-automated approach, similar to Dugdale et al., (2010), to georeference individual sUAS images.

The first step is to export undistorted images from PhotoScan Pro (Agisoft LLC). These images have been corrected for the lens distortion effect as calibrated by the Photoscan Bundle adjustment (see Carbonneau and Dietrich, 2017 for a discussion of camera calibration in Photoscan). Carbonneau and Dietrich (2017) found that at the edges, Phantom 3 images have a radial displacement on the order of 100 pixels. This could add significant georeferencing errors and it is preferable to correct this lens effect and export the individual images. Next, we export camera locations and orientations from PhotoScan. This information gives the adjusted XYZ positions along with yaw (azimuth), pitch and roll for each camera as calculated by the photogrammetric bundle adjustment. Our experience strongly suggests that this information is more accurate than that which can be obtained from drone flight logs. The camera parameters, along with the single images and the orthomosaic are then used in a MATLAB code for automatic registration point generation. The core principle of this algorithm is to find matching points shared by the georeferenced orthomosaic and single images. Once matched, the position information of a point can be extracted from the orthomosaic in order to define a 2D ground control point. Multiple points can then be used to georeference the single image with a standard affine transform. We begin by using the camera position and yaw information to roughly locate the image with respect to the orthomosaic. This approximate position is used to constrain the search area of the *OpenSURF* keypoint descriptor used above. The sensitivity threshold of the *OpenSURF* algorithm was manually adjusted to very high severity in order to minimise the presence of false positive matches and to

deliver between 5 and 15 matches between the orthomosaic and each given single image. Once adjusted, the algorithm extracts the spatial position of the matched points and outputs a control points file in the open-source format used by the QGIS software (version 2.18). It was found that, despite the severity of the matching criteria used in the *OpenSURF* algorithm, false positives persist. We therefore used the georeferencing tool in QGIS to manually eliminate these false positives. Once developed, this process allows for a user to georeference an image in 3-4 minutes. We georeferenced 10 images covering the gravel bar for each sUAS.

The main drawbacks of this method of georeferencing are that; (1) we do not account for roll and pitch angles of the sUAS when each image was captured, and (2) the process is 2D and we do not account for the slope of the bank. Therefore, images that were off-nadir are expected to have higher residual errors and areas on top of the bank, in the vegetated areas, are expected to have even higher errors. The quality of the outputs was checked by finding 3 distinct gravel-bar features in each sUAS image. For each feature, we measure the 2D distance between the position of the feature in the orthomosaic and the single image. If the single image is perfectly co-registered to the orthomosaic, this distance should be zero. We then conducted an additional check on the quality of the spatial resolution of each image as derived from the georeferencing process. We used the exported camera locations, focal length and the point cloud of the ground in order to derive the spatial resolution according to Equation 2, where Rs is the spatial resolution, H is the flying height, p is the linear size of 1 pixel on the camera detector and f is

the focal length. Here we use the adjusted focal length exported from PhotoScan after the bundle adjustment process. We then compare this measurement of spatial resolution to the one derived from the georeferencing process which is directly written as a term in the affine transformation matrix saved in the world file.

$$Rs = \frac{Hp}{f}$$

Equation 2.

The LOOCV grain size mapping algorithm used above was then adapted to single images. This involved pre-calculating the texture for all individual sUAS images. We used the same range of kernel window sizes as above: 5 to 101 pixels in steps of 4 pixels. We then run the adapted LOOCV algorithm. This starts by excluding the first of the 30 ground truth plots. The algorithm then loads the first of 10 sUAS images and, by using the surveyed location, determines which plots were captured in this image. We then apply an exclusion criterion of twice the current texture kernel size in order to eliminate plots which fall too close to the edge of the image and whose texture might be affected by edge effects. The spatial resolution of the image is then used to normalise the D_{50} values for each visible plot. Local textural entropy values for the first kernel size (5 pixels) are then extracted for each visible plot and stored as a table of dimensionless grain size against texture. The algorithm then moves to the next image and again locates the visible plots. The D_{50} values

are normalised by the new image scale. Readers should note that the normalised D_{50} value for a given plot visible in more than 1 image will be different for successive images as the image scale varies. Once again, textures are extracted and the table of texture vs. normalised D_{50} is expanded and stored. Once all images and plots have been processed, the algorithm fits a linear model of normalised D_{50} vs. texture and attempts to predict the excluded plot with the texture from each image where it is visible. This means that each excluded plot may be associated with more than 1 prediction. Once the first LOOCV prediction is calculated, the second plot is excluded and the entire process is repeated. Once all 30 plots have been excluded in the LOOCV loop, the kernel size is iterated, the LOOCV loop is reset, and the entire process is again repeated for kernel sizes up to 101 pixels, in steps of 4 pixels. This algorithm is applied to the single images from both the F550 and P3P sUAS. The results are analysed by identifying the calibration with the strongest fit (via the adjusted R^2) and the corresponding quality of the predictions. Figure 5 gives a workflow.

Grain size mapping: Roughness-based approach

An overview of the grain size mapping approach using roughness, based on the method first presented by Woodget (2015), is presented in Figure 6. We begin by detrending and cleaning the cloud to remove the unwanted effects of local slope and noise within the cloud respectively, which might otherwise adversely impact roughness calculations. Both operations are conducted within the open source CloudCompare software (www.danielgm.net/cc/): detrending by fitting a 3D plane to the cloud and cleaning by applying the in-built noise filter with a radius of 0.15m and

an absolute maximum error of 0.3m, based on *a priori* knowledge of typical grain sizes at this site. A visual sensitivity check was used to ensure that sufficient noise removal occurred whilst not sacrificing topographic detail.

Next, we select the kernel size which will be used to compute roughness using CloudCompare's inbuilt tool. This tool defines roughness as the shortest distance between each point in the cloud and the ordinary least-squares best fitting plane computed on the nearest neighbours of that point within a spherical kernel of a user-specified size. We selected a starting roughness kernel size of 0.1m, based on *a priori* knowledge of the typical grain size and point cloud density at this site, which was then used to compute roughness for every point in the cloud. The only time when roughness is not computed for a point is when less than four points fall within the kernel, as a minimum of three points are required for computing the least-squares plane. Next, we compute the mean roughness of all points falling within each ground truth plot, and regress this against the equivalent A- and B-axis grain size statistics (i.e. mean, D50, D84) for each plot. We repeat this process multiple times, incrementing the kernel size by 0.05m each time, up to a maximum kernel size of 0.5m. Linear regression of mean roughness and grain sizes statistics is then possible for all ground truth sample plots and all kernel sizes, to find the best calibration relationship between these two variables.

Finally, we validate the best calibration relationship using jack-knifing (Quenouille, 1949; Tukey, 1958). This is an iterative validation approach which excludes one ground truth plot with each iteration. It uses the regression relationship computed from all remaining plots to predict the grain size from the roughness value of the excluded plot. This is repeated until all plots have been excluded and their grain size predicted. A comparison of observed versus predicted grain sizes is then possible,

permitting an assessment of the strength of the predictive relationship and the calculation of error metrics, including mean error (accuracy), standard deviation of error (precision) and maximum error.

Results

Quantifying the impact of camera gimbals

Table 1 details the PhotoScan image quality and entropy values computed for each sUAS image set from Survey 1. Overall, it is clear that absolute image quality is lower for those images acquired using the F550 with no gimbal, than for those images acquired using the P3P sUAS with a three-axis gimbal, as indicated by lower F550 values for the minimum PhotoScan image quality.

In addition, we observe a greater range in image quality within the F550 imagery compared to the P3P, as indicated by the PhotoScan image quality range, the entropy range, the entropy standard deviation and the average and standard deviation of difference in entropy between the best quality and other images (mean error and standard error). This greater range of blur within the F550 images is demonstrated in Figure 7, where we observe a greater scatter in the arrangement of points and a lower R^2 value when compared to the P3P data. The tight clustering of points obtained from the P3P imagery and high R^2 value are indicative of consistently sharp, higher quality imagery. Furthermore, whilst maximum image entropy values for the two sUAS set-ups are similar (Table 1), **Error! Reference source not found.**7 shows that values greater than 7 are only seen consistently within the P3P imagery. These results indicate that the use of a gimbal (within the P3P set up) is paramount for collecting consistently high quality, sharp imagery. These results do

not provide information about the effects of using different gimbal types, but rather provide the first quantitative evidence of the effect of (a) using a gimbal, versus (b) not using a gimbal, on the quality of imagery which can be captured from a sUAS.

Grain size mapping: Image-based approaches

Figure 8 shows the results for the orthomosaic approach applied to the F550 data and Figure 9 shows the same results for the P3P data. Calibration performance (part A of each figure) is better for the P3P with a maximum R^2 of approximately 0.48 for a kernel size of 69 pixels. In contrast, the best calibration for the F550 had an R^2 of only about 0.32 for a kernel size of 41 pixels. We define error as the difference between predicted and observed grain sizes. A negative error means an under-prediction. Validation performance is very similar with a significant underestimation of grain sizes (mean error of -34mm in both cases) and a standard deviation of error of 8.8mm and 8.7mm for the F550 and the P3P respectively. Validation slopes in part C of both figures are low (<0.65) and indicate a relatively poor prediction of grain sizes. Given the marked difference in image qualities displayed in Table 1 and Figure 7, these results suggest that the orthorectification process significantly degrades the consistent textures in the single P3P images.

In the case of the single image approach, the georeferencing quality check revealed mean errors of 224mm and 91mm, and standard deviations of error of 209mm and 88mm for the F550 and P3P sUAS respectively. Maximum errors were 581mm and 833mm for the P3P and the F550, respectively. Despite the larger errors for the F550, which are to be expected in the absence of a gimbal, both mean errors are significantly smaller that the 1m size of the ground truth plots. Verification of the

spatial resolution revealed that the georeferencing process resulted in scales that were very consistent with those obtained with Equation (2). For the P3P, the difference in spatial resolutions was on average 0.04mm with a standard deviation of 0.13mm. For the F550, the difference in spatial resolutions was on average 0.06mm with a standard deviation of 0.35mm. When compared to the average spatial resolution, the standard deviation of differences equates to 1.3% and 3.1% for the P3P and F550, respectively. Closer examination of the data in Figure 2 shows that, even for the P3P flights which were programmed to fly at a set altitude of 20m, there is an actual range in flight altitudes of +/- c. 2m. At altitudes of c. 20m, this represents a variance of scale of nearly 15%. The case is more severe for the F550 with a range in flight altitudes of +/- c. 10m for a mean flight altitude of 34m. This demonstrates that calculating a single spatial resolution based on the average flying altitude would be highly inaccurate.

Figure 10 presents the result for the F550 while Figure 11 presents the results for the P3P for the single image approach. For the F550, the results are poor with low calibration R^2 values and a very high scatter for the validation associated with a mean error of 12.4mm and a standard error of 9.7mm. The validation slope is 0.5, once again indicating proportional under-estimation. Results for the P3P are significantly better. Calibration R^2 reaches 0.6 for window sizes of 61 pixels. The best validation now has a mean error of 0.02mm and a standard error 0f 6.9mm. Crucially, the slope of the best validation is 0.97. However, despite these positive indicators, the maximum error remains high at 16.5mm.

Grain size mapping: Roughness-based approaches

Figure 12 shows the results for the point cloud roughness approach applied to the F550 data and Figure 13 shows the same results for the P3P data. Calibration performance (part A of each figure) is better for the P3P with a maximum R^2 of approximately 0.6 for a kernel size of 0.4m. In contrast, the best calibration for the F550 has an R^2 of only about 0.39 for a kernel size of 0.35m. Validation performance is markedly different between the P3P and F550, with all error metrics for the P3P being significantly lower (i.e. better) than those obtained for the F550 (Table 2). Validation slopes in part C of both figures are low and indicate a relatively poor prediction of grain sizes, although the slope for the P3P data (0.59) is notably higher than that for the F550 data (0.33).

Summary of grain size mapping results

Table 2 provides a summary comparing key metrics across methods and for both sUAS. Our new single image texture method produces stronger calibration and validation results than either the orthomosaic or roughness methods, when used on data collected by the P3P with a 3-axis gimbal. The roughness method tends to perform better than the orthomosaic approach when applied to the P3P data, with a stronger calibration R^2 and notably lower mean and maximum errors. The results from the F550 sUAS are almost always inferior to the P3P results, regardless of the method. No single method consistently outperforms the other methods where no gimbal is used on the F550 sUAS.

Discussion

Our results show that our novel approach of using single sUAS images, acquired from a 3-axis stabilised gimbal and calibrated with grain sizes normalised by individual image scale, delivered the optimal grain size mapping performance for our study site. This new method outperformed an advanced roughness-based method and a more traditional image-based method reliant on orthoimagery to control image scale. Our results also demonstrate the critical importance of mechanical image stabilisation for grain size mapping or any other analysis method which relies on image texture. We focus our discussion on the following key points; the poor performance of the roughness mapping in comparison with existing research, the excellent performance of our novel single image approach, the need for camera gimbals and the implications of these findings for future work on grain size mapping.

The sUAS-SfM point cloud roughness method was originally developed in response to concerns about the effects of blurring within sUAS imagery (Woodget, 2015; Woodget and Austrums, 2017). Initial results have shown promise, yet applications have been focussed on sites where grain size is clearly expressed in three dimensions (i.e. in the topographic signature) and where the range in grain size is c. 0.16m (D_{84} of B axis). At our site, however, particles are imbricated and grain size range is notably smaller (c. 0.07m for D_{84} of B axis). As a result, we observe that grain size is not being expressed in 3D to the same extent and therefore roughness does not readily calibrate with grain size. This is some of the first evidence to suggest that the topographic roughness approach may not have universal applicability. The level of imbrication is significant to the success of this approach. Furthermore, very recently, others have suggested that grain shape also impacts on the success of roughness based grain size quantification methods (Pearson et al.,

2017). Clearly, further work to quantify the range in grain size, shape and level of imbrication where the roughness method performs successfully is required.

In contrast, our single image method performs exceptionally well (when a gimbal is used). For studies at the micro and mesoscale, this novel method produces results of a spatial resolution, accuracy, precision and grain size predictive strength (i.e. slope of observed versus predicted regression) which is at least as good as, and sometimes better than, all existing remote-sensing based grain size quantification measures, including close range photosieving (e.g. Butler et al., 2001; Graham et al., 2005a; Graham et al., 2005b), statistical image analysis (e.g. Rubin, 2004; Buscombe, 2008; Buscombe and Masselink, 2009; Buscombe et al., 2010; Buscombe and Rubin, 2012; Buscombe, 2013) and terrestrial laser scanning (e.g. McEwan et al., 2000; Entwistle and Fuller, 2009; Heritage and Milan, 2009; Hodge et al., 2009; Brasington et al., 2012; Milan and Heritage, 2012; Rychov et al., 2012). Furthermore, it is more robust to imbrication because the particles on the top layer of an imbricated bed will have a significant portion of their edges, in the two-dimensional AB plane, uncovered. This means that these edges will produce shadows which is the mechanism postulated by Carbonneau et al. (2004) which permits the correlation of image texture with grain size. In addition, because grain size is inferred from the two dimensional patterns of image brightness, image-based approaches are less affected by variability in grain shape. For example, where flat, disc-like particles produce little topographic signature, and therefore minimal roughness within the point cloud, their 2D appearance within the image is unaffected and thus the calibration with texture is uncompromised. This would suggest that image-based approaches (single image or orthomosaic) should always provide a more robust method of grain size mapping than roughness-based methods.

However, this is not borne out by existing research where sUAS-SfM derived orthomosaics are compared with roughness approaches (Woodget and Austrums, 2017), nor within the results we present here. The processing of single sUAS images into orthomosaics using SfM modifies the patterns of image brightness in a way which compromises the texture-grain size relationship. For the first time, we have presented a single image method which circumvents this problem and promises wider applicability for use on sUAS imagery. Further testing at a range of contrasting locations is required however. At present, the complexity of this approach may present barriers to applicability in terms of the required technical expertise, time and processing power. For example, whilst the georeferencing of 10 images took us 30-40 minutes to process, it would not be unreasonable to expect the collection of more than 1000 images during a survey of numerous gravel bars on a longer stretch of river. This has become possible recently given the longer battery lives of the sUAS which are now available, and the efficient image acquisition missions now made possible by flight planning apps such as Ground Station Pro (DJI, 2017) or Litchi (VC Technology Ltd, 2017). In such scenarios, it is hoped that future developments of SfM packages would include the option to export georeferenced individual images without orthocorrection.

Our results also provide evidence that without the use of a gimbal, grain size mapping results will be poor, regardless of the choice of method. This is of particular significance to our single image method, where we have shown that the outputs for the F550 drone remain of poor quality even when dimensionless grain sizes are used to account for changes of image scale and spatial resolution. That is, we observe a deterioration of mean error by more than two orders of magnitude when a gimbal is not used. A notable deterioration in quality metrics are also observed for

our roughness method when the gimbal is not used. This provides the first quantitative evidence of the implications of camera stabilisation for the acquisition of aerial imagery from sUAS. It also provides evidence that camera stabilisation may be responsible for the variable success of sUAS grain size mapping methods reported previously (de Haas et al., 2014; Tamminga et al., 2015; Vázquez-Tarrío et al., 2017; Woodget and Austrums, 2017). Fortunately, many newer sUAS are equipped with 3-axis stabilisation gimbals as standard, driven by requirements of the video filming community in particular. Such developments may obviate the need for methods of detecting and eliminating blur from imagery post-acquisition, and we suggest that particle size quantification should not be undertaken using a sUAS which does not have a gimbal mounted sensor.

Further work on grain size quantification from sUAS should focus on developing an approach which works regardless of whether grain size is expressed in 2D or 3D. Our new single image method may be capable of this, however further quantitative evidence at a range of sites is needed. It will be of interest to those requiring a quick and easy approach to know how our single image method compares to the less complex roughness method at sites where 3D expression of grain size is stronger. Alternatively, improvements to the speed and automation of georeferencing single images would be advantageous, as would dedicated experiments within submerged parts of the fluvial environment. As an ultimate goal, a method which removes the need for ground truth calibration plots altogether would be of great value, as this often consumes the greatest time and effort during the data acquisition phase.

Conclusion

Within this paper we have developed and presented a comprehensive approach to particle sizing from sUAS within a fluvial setting. This has comprised quantifying the

impacts of camera gimbals on image quality and subsequent grain size estimation, and the adaptation of a traditional image-based texture method for use with single images acquired from sUAS. Our key findings demonstrate that the use of a 3-axis stabilising gimbal is paramount for accurate and precise grain size estimation from sUAS data. Furthermore, our novel approach using the texture of single sUAS images with dimensionless calibration grain sizes has outperformed the equivalent results of an orthophoto texture approach and a method based on the roughness of SfM point clouds. Whilst improvements in the usability and efficiency of our new method are required before more widespread use is possible, our results clearly demonstrate proof of concept for our method which compare favourably to existing grain size mapping methods based on remote sensing data. Further testing is required to confirm the wider applicability of this approach and in particular, its ability to predict grain size in a range of environments, over a range of scales, over a range of grain shapes and at different imbrication levels.

Acknowledgements and author contributions

We would like to thank Carlos Puig-Mengual for assistance in the field and ground truthing of grains in GIS. AW and PC conceived of the study. AW implemented the roughness-based grain size analysis method and wrote 70% of the paper. CF performed the texture stability analysis and wrote 10% of the paper. PC developed the concept of dimensionless grain sizes, implemented all texture-based grain size analysis methods and wrote 20% of the paper.

References

Adams, J. 1979. Gravel size analysis from photographs. Journal of the Hydraulics Division, Proceedings of the American Society of Civil Engineers, 105, HY10: 1247-1255

Agisoft LLC (2016) *Agisoft PhotoScan User Manual: Professional Edition, Version 1.2*, Agisoft

Baewert, H., Bimböse, M., Bryk, A., Rascher, E., Schmidt, K.H. and Morche, D. 2014. Roughness determination of coarse grained alpine river bed surfaces using terrestrial laser scanning data. Zeitschrift für Geomorphologie Supplementary Issues 58 (1): 81-95

Black, M., Carbonneau, P.E., Church, M. and Warburton, J. 2014. Mapping sub-pixel fluvial grain sizes with hyperspatial imagery. Sedimentology 61 (3): 691-711

Brasington, J., Vericat, D. and Rychov, I. 2012. Modeling river bed morphology, roughness, and surface sedimentology using high resolution terrestrial laser scanning. Water Resources Research 48 W11519, doi: 10.1029/2012WR012223

Buscombe, D. 2008. Estimation of grain size distributions and associated parameters from digital images of sediment. Sedimentary Geology 210: 1-10

Buscombe, D. 2013. Transferable wavelet method for grain-size distribution from images of sediment surface and thin section, and other natural granular patterns. Sedimentology 60 (7): 1709-1732.

Buscombe, D. and Masselink, G. 2009. Grain-size information from the statistical properties of digital images of sediment. Sedimentology 56: 421-438

Buscombe, D. Rubin, D.M. and Warrick, J.A. 2010. A universal approximation of grain size from images of noncohesive sediment. Journal of Geophysical Research 115 F02014 doi: 10.1029/2009JF001477

Buscombe, D. and Rubin, D.M. 2012. Advances in the simulation and automated measurement of well sorted granular material: 2. Direct measures of particle properties. Journal of Geophysical Research: Earth Surface 117 (F2)

Butler, J.B., Lane, S.N, and Chandler, J.H. 2001. Automated extraction of grain-size data from gravel surfaces using digital image processing. Journal of Hydraulic Research 39 (4): 519-529

Carbonneau, P.E., Bergeron, N.E. and Lane, S.N. 2005a. Texture-based segmentation applied to the quantification of superficial sand in salmonids river gravels. Earth Surface Processes and Landforms 30: 121-127

Carbonneau, P.E., Lane, S.N. and Bergeron, N. 2004b. Catchment-scale mapping of surface grain size in gravel bed rivers using airborne digital imagery. Water Resources Research 40, W07202, doi: 10.1029/2003WR002759

Carbonneau, P.E. 2005. The threshold effect of image resolution on image-based automated grain size mapping in fluvial environments. Earth Surface Processes and Landforms 30 (13) : 1687-1693

Carbonneau, P.E., Bergeron, N. and Lane, S.N. 2005. Automated grain size measurements from airborne remote sensing for long profile measurements of fluvial grain sizes. Water Resources Research 41, W11426, doi:10.1029/2005WR003994

Carbonneau, P.E. and Dietrich, J.T. 2017. Cost-effective non-metric photogrammetry from consumer-grade sUAS: Implications for direct georeferencing of structure from motion photogrammetry. Earth Surface Processes and Landforms 42 (3): 473-486

Church, M.A. McLean, D.G. and Wolcott, J.F. 1987. River bed gravels: Sampling and Analysis, In Thorne, C.R., Bathurst, J.C. and Hey, R.D. (Eds) Sediment Transport in Gravel-bed Rivers, John Wiley and Sons, Chichester

De Haas, T., Ventra, D., Carbonneau. P. and Kleinhans, M.G. 2014. Debris flow dominance of alluvial fans masked by runoff reworking and weathering. Geomorphology 217: 165-181

Detert, M. and Weitbrecht, V. 2012. Automatic object detection to analyse the geometry of gravel grains – a free, standalone tool. In Muñoz, R.E.M (Eds) River Flow 2012. CRC Press/Balkema, Leiden

Dugdale, S.J., Carbonneau, P.E. and Campbell, D. 2010. Aerial photosieving of exposed gravel bars for the rapid calibration of airborne grain size maps. Earth Surface Processes and Landforms 35: 627-639

Eltner, A., Kaiser, A., Castillo, C., Rock, G., Neugirg, F. and Abellán, A. 2016. Image-based reconstruction in geomorphometry – merits, limits and developments. Earth Surface Dynamics 4: 359-389

Entwistle, N.S. and Fuller, I.C. 2009. Terrestrial laser scanning to derive the surface grain size facies character of gravel bars. In Heritage, G.L. and Large, A.R.G. (Eds) Laser Scanning for the Environmental Sciences, Wiley-Blackwell, London

Fonstad, M.A., Dietrich, J.T., Courville, B.C., Jensen, J.L. and Carbonneau, P.E. 2013. Topographic structure from motion: a new development in photogrammetric measurement. Earth Surface Processes and Landforms 38 (4): 421-430

Graham, D.J., Reid, I. and Rice, S.P. 2005a. Automated sizing of coarse-grained sediments: image- processing procedures. Mathematical Geology 37(1): 1-28

Graham, D.J., Rice, S.P. and Reid, I. 2005b. A transferable method for the automated grain sizing of river gravels. Water Resources Research 41, W07020, doi:10.1029/2004WR003868

Haralick, R.M., Shanmugam, K. and Dinstein, I. 1973. Textural features for image classification. IEEE Transactions on Systems, Man and Cybernetics SMC-3 (6): 610-621

Heritage, G.L. and Milan, D.J. 2009. Terrestrial laser scanning of grain roughness in a gravel-bed river. Geomorphology 113: 4-11

Hey, R.D. and Thorne, C.R. 1983. Accuracy of surface samples from gravel bed materials. Journal of Hydraulic Engineering 109 (6): 842-851

Hodge, R., Brasington, J. and Richards, K. 2009. In situ characterization of grain-scale fluvial morphology using Terrestrial Laser Scanning. Earth Surface Processes and Landforms 34: 954-968

Ibbeken, H. and Schleyer, R. 1986. Photo-sieving: a method for grain size analysis of coarse-grained, unconsolidated bedding surfaces. Earth Surface Processes and Landforms 11: 59-77

Kroon, D. (2010) *OpenSURF*, MathWorks, https://uk.mathworks.com/matlabcentral/fileexchange/28300-opensurf--including-image-warp- [accessed 02/05/2017]

Leopold, L.B. 1970. An improved method for size distribution of stream bed gravel. Water Resources Research 6 (5): 1357-1366

McEwan, I. K., Sheen, T.M., Cunningham, G.J. and Allen, A.R. 2000. Estimating the size composition of sediment surfaces through image analysis. Proceedings of the Institution of Civil Engineers – Water and Maritime Engineering 142: 189–195

Milan, D.J. and Heritage, G.L. 2012. LiDAR and ADCP use in gravel-bed rivers: Advances since GBR6. In Church, M., Biron, P. and Roy, A. (Eds) Gravel-bed Rivers: Processes, Tools, Environments, Wiley-Blackwell, Chichester

Newson, M.D. and Newson, C.L. 2000. Geomorphology, ecology and river channel habitat: mesoscale approaches to basin-scale challenges. Progress in Physical Geography 24 (2): 195-217

Pearson, E., Smith, M.W. Klaar, M.J. and Brown, L.E. 2017. Can high resolution 3D topographic surveys provide reliable grain size estimates in gravel bed rivers? Geomorphology 293: 143-155

Quenouille, M.H. 1949. Approximate tests of correlation in time-series. Journal of the Royal Statistical Society Series B 11: 68-84

Rice, S. and Church, M. 1996. Sampling surficial fluvial gravels: the precision of size distribution percentiles estimates. Journal of Sedimentary Research 66 (3): 654-665

Rubin, D.M. 2004. A simple autocorrelation algorithm for determining grain size from digital images of sediment. Journal of Sedimentary Research 74 (1): 160-165

Rychov, I., Brasington, J. and Vericat, D. 2012. Computational and methodological aspects of terrestrial surface analysis based on point clouds. Computers and Geosciences 42: 64-70

Sime, L. C. and Ferguson, R. I. 2003. Information on grain sizes in gravel-bed rivers by automated image analysis. Journal of Sedimentary Research 73 (4): 630-636

Smith, M.W., Carrick, J.L. and Quincey, D.J. 2015. Structure from motion photogrammetry in physical geography. Progress in Physical Geography 40 (2): 247-275

Tamminga, A., Hugenholtz, C., Eaton, B. and LaPointe, M. 2015. Hyperspatial remote sensing of channel reach morphology and hydraulic fish habitat using an unmanned aerial vehicle (UAV): A first assessment in the context of river research and management. River Research and Applications 31 (3): 379-391

Tukey, J.W. 1958. Bias and confidence in not-quite large samples. Annals of Mathematical Statistics 29: 614

Vázquez-Tarrío, D. Borgniet, L., Liébault, F. and Recking, A. 2017. Using UAS optical imagery and SfM photogrammetry to characterize the surface grain size of gravel bars in a braided river (Vénéon River, French Alps). Geomorphology 285: 94-105

Verdú, J.M., Batalla, R.J. and Martinez-Casasnovas, J.A. 2005. High-resolution grain-size characterisation of gravel bars using imagery analysis and geo-statistics. Geomorphology 72: 73-93

Wentworth, C.K. 1922. A scale of grade and class terms for clastic sediments. Journal of Geology 30: 377-392

Westoby, M.J., Brasington, J., Glasser, N.F., Hambrey, M.J. and Reynolds, J.M. 2012. 'Structure –from-Motion' photogrammetry: A low-cost, effective tool for geoscience applications. Geomorphology 179: 300-314

Wolman, M.G. 1954. A method of sampling coarse river-bed material. Transactions of the American Geophysical Union 35 (6): 951-956

Woodget, A.S. 2015. Quantifying physical river habitat parameters using hyperspatial resolution UAS imagery and SfM-photogrammetry. Unpublished PhD Thesis, University of Worcester, UK.

Woodget, A.S. and Austrums, R. 2017. Subaerial gravel size measurement using topographic data derived from a UAV-SfM approach. Earth Surface Processes and Landforms 42 (9): 1434-1443

Woodget, A.S., Austrums, R., Maddock, I.P. and Habit, E. 2017. Drones and digital photogrammetry: from classifications to continuums for monitoring river habitat and hydromorphology. WIREs Water 4:4 doi: 10.1002/wat2.1222

*Table 1. Image quality for both UAVs, as determined by PhotoScan and the entropy values of selected points. *denotes that measure relates to the linear regression between highest quality image and all other images, as shown in Figure 7.*

Impact measure	3-axis gimbal (P3P)	No gimbal (F550)
PhotoScan image quality minimum (worst)	0.828	0.582
PhotoScan image quality range	0.006	0.221
Maximum entropy	7.280	7.070
Entropy range	4.020	5.680
Entropy standard deviation	0.770	0.850
*Average difference in entropy (mean error)	0.033	0.442
*Standard deviation of difference in entropy (standard error)	0.124	0.508
*R^2	0.902	0.652
*Slope	0.974	0.902

Table 2. Summary of key quality metrics for orthomosaic, single image and roughness methods performed using imagery acquired by two different sUAS/gimbal set-ups.

Quality Metric	Method	3-axis gimbal (P3P)	No gimbal (F550)
Strongest calibration R^2	Orthomosaic	0.48	0.32
	Single Image	0.69	0.14
	Roughness	0.60	0.39
Predicted v. observed slope	Orthomosaic	0.59	0.64
	Single Image	0.97	0.50
	Roughness	0.59	0.33
Mean error (mm)	Orthomosaic	-34.00	-34.10
	Single Image	0.02	12.40
	Roughness	0.07	0.30
Standard deviation of error (mm)	Orthomosaic	8.80	8.70
	Single Image	6.90	9.70
	Roughness	10.15	23.63
Maximum error (mm)	Orthomosaic	53.40	49.30
	Single Image	16.50	33.90
	Roughness	19.46	53.81

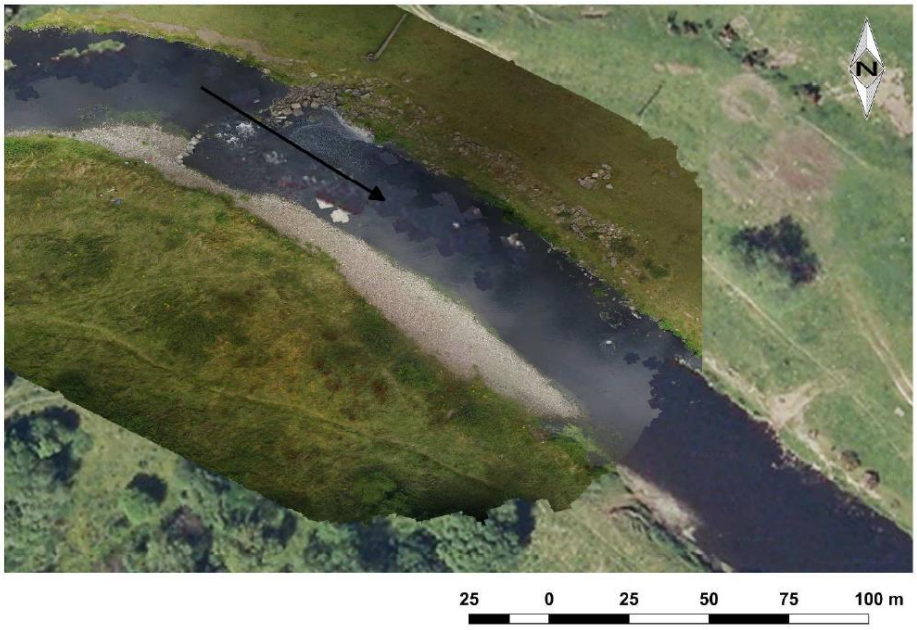

Figure 1. Study site. Orthophoto generated from Phantom 3 Pro imagery is shown overlying Google Quickmap imagery. The arrow indicates the direction of flow.

1
2

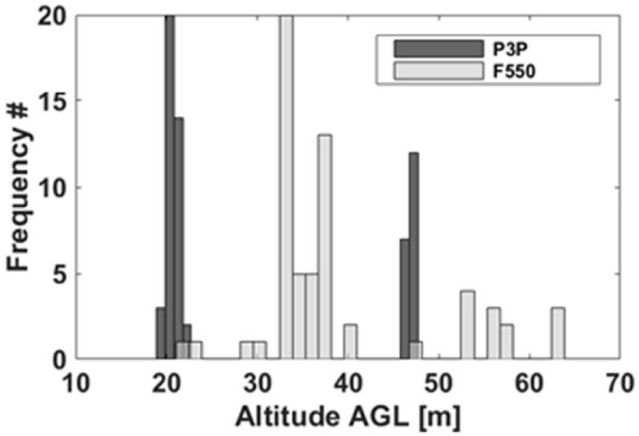

Figure 2. Flight altitudes above ground level (AGL) for the F550 and the P3P surveys.

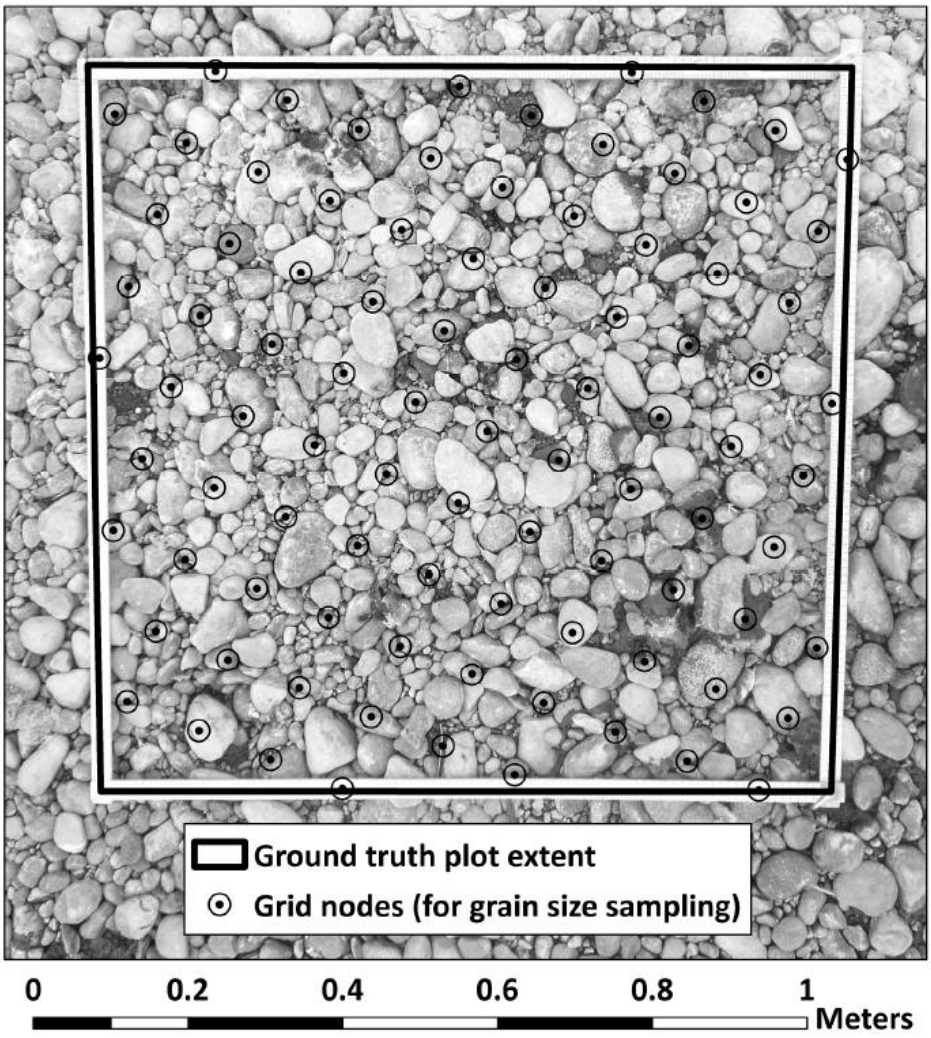

Figure 3. Example of a ground truth sample plot.

1
2
3

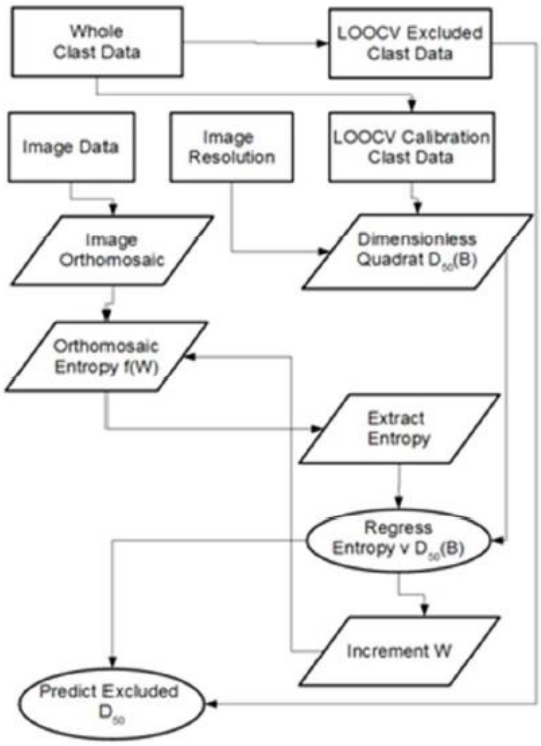

Figure 4. Texture mapping method, as applied to the orthomosaics computed from the P3P and F550 imagery acquired during Survey 2. W = window or kernel size, B = B axis grain size.

1
2

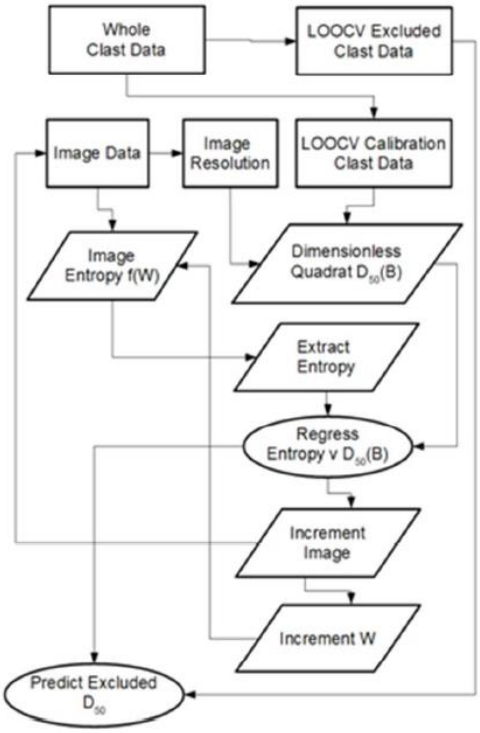

Figure 5. Texture mapping method, as applied to the single images acquired from the P3P and F550 sUAS during Survey 2. W = window or kernel size, B = B axis grain size.

1
2
3

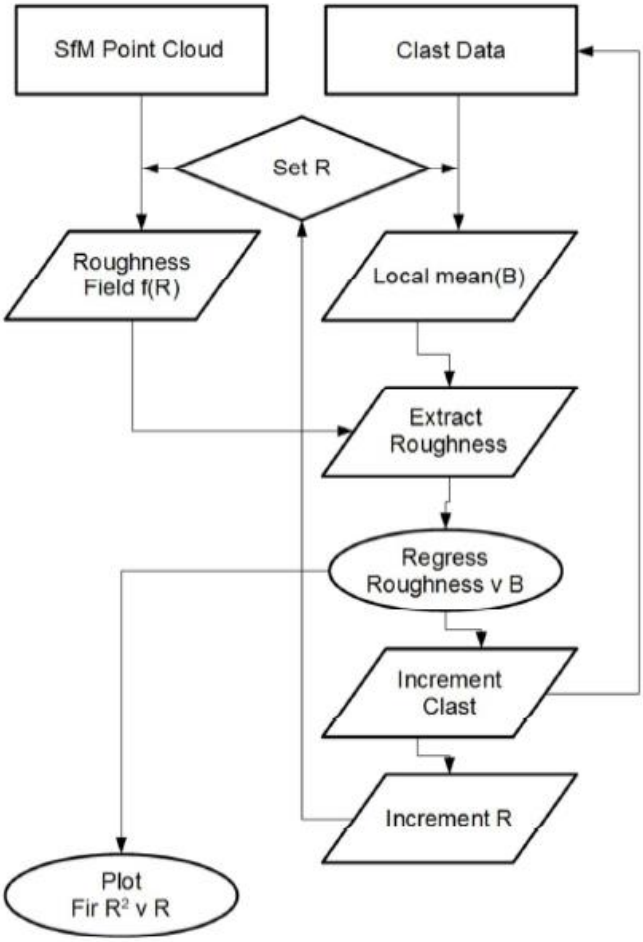

Figure 6. Roughness method, as applied to dense point clouds. K = radius size of spherical roughness kernel.

1
2
3

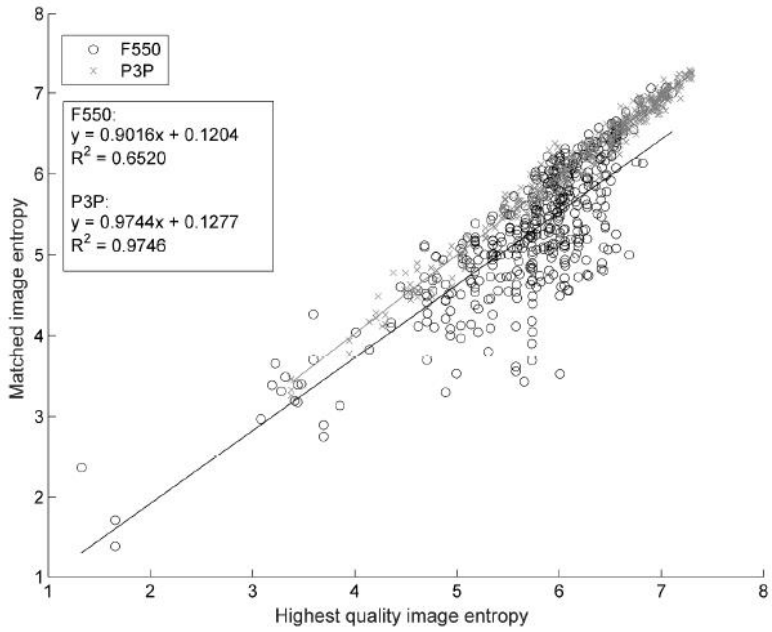

Figure 7. Linear regression of entropy of highest quality image with matched points from all other images, for the F550 and P3P sUAS image sets acquired during Survey 1.

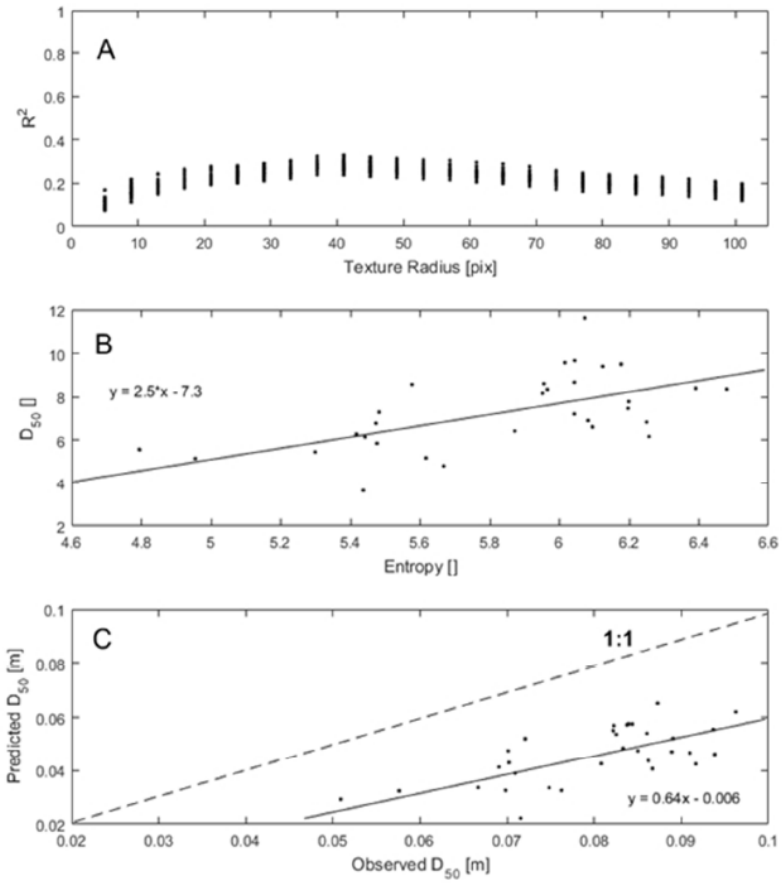

Figure 8. Grain size mapping quality for the F550 using the orthomosaic A) Calibration model quality. Results of each of the 30 leave-one-out calibrations are plotted against texture radius. B) Best calibration result. C) Best validation result with a mean error of -34.1 mm and a standard deviation of error of 8.7mm. Maximum error is 49.3mm.

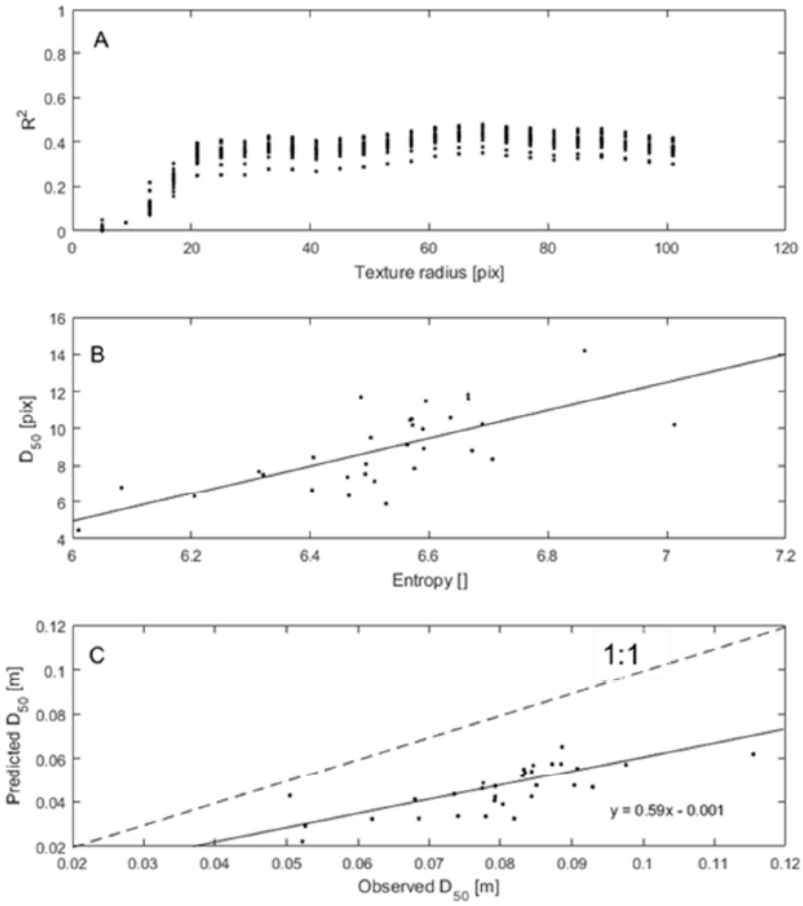

Figure 9. Grain size mapping quality for the P3P using the orthomosaic. A) Calibration model quality. Results of each of the 30 leave-one-out calibrations are plotted against texture radius. B) Best calibration result. C) Best validation result with a mean error of -34.0 mm and a standard deviation of error of 8.8mm. Maximum error is 53.4 mm.

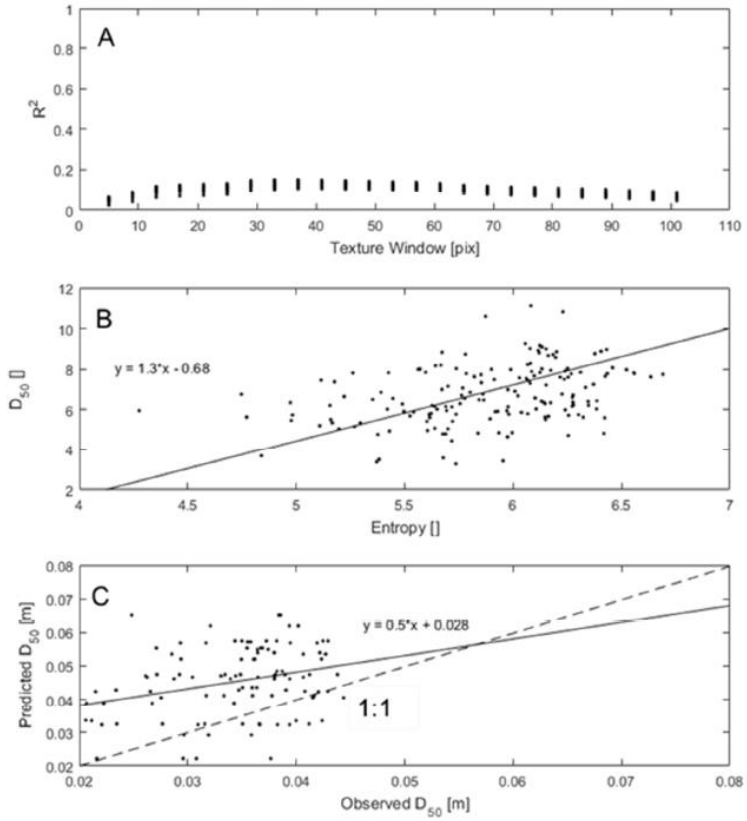

Figure 10. Grain size mapping quality for the F550 using single images. A) Calibration model quality. Results of each of the 30 leave-one-out calibrations are plotted against texture radius. B) Best calibration result. C) Best validation result with a mean error of 12.4 mm and a standard deviation of error of 9.7mm. Maximum error is 33.9 mm.

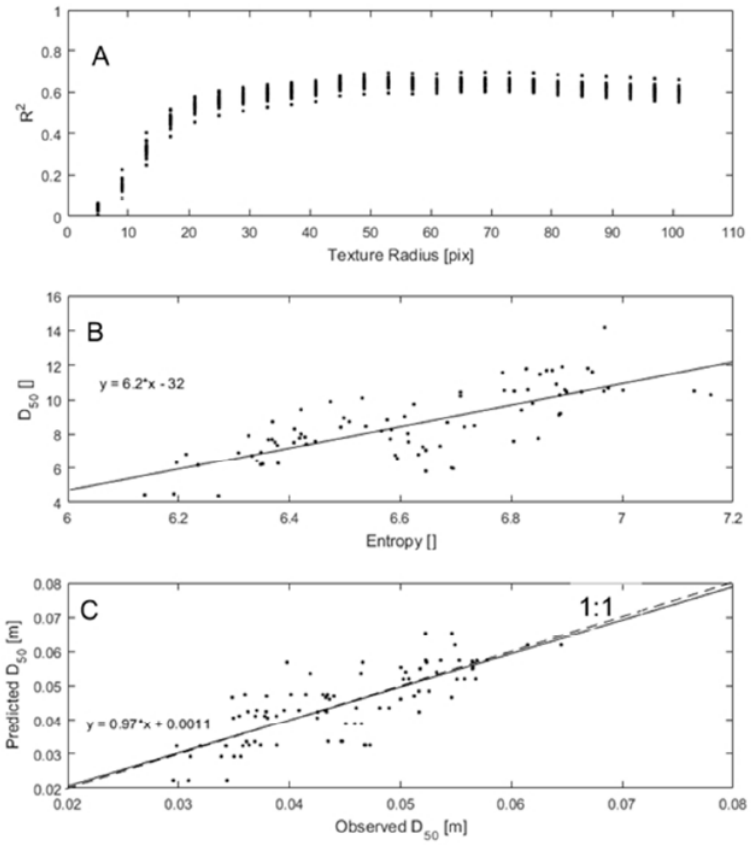

Figure 11. Grain size mapping quality for the P3P using single images. A) Calibration model quality. Results of each of the 30 leave-one-out calibrations are plotted against texture radius. B) Best calibration result. C) Best validation result with a mean error of 0.02 mm and a standard deviation of error of 6.9mm. Maximum error is 16.5 mm.

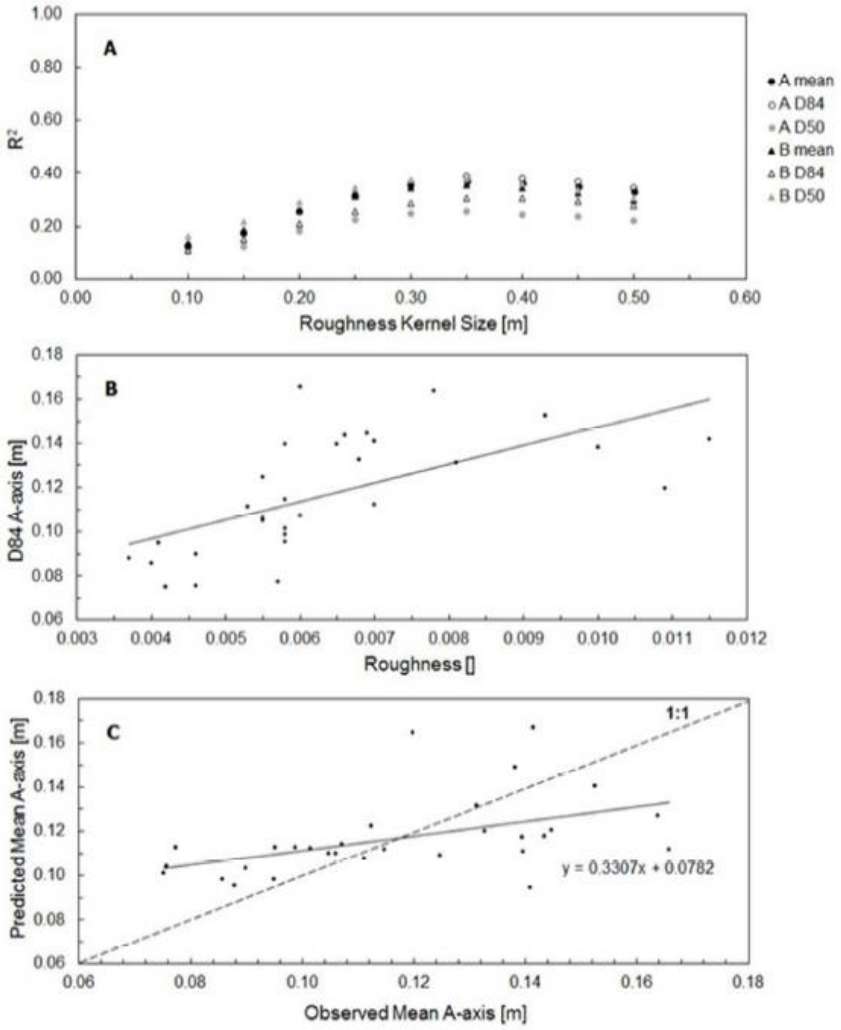

Figure 12. Grain size mapping quality for the F550 using point cloud roughness. A) Calibration model quality. Results for each measure of grain size are plotted against roughness kernel size. B) Best calibration result. C) Best validation result with a mean error of 0.3 mm and a standard deviation of error of 23.63 mm. Maximum error is 53.81 mm.

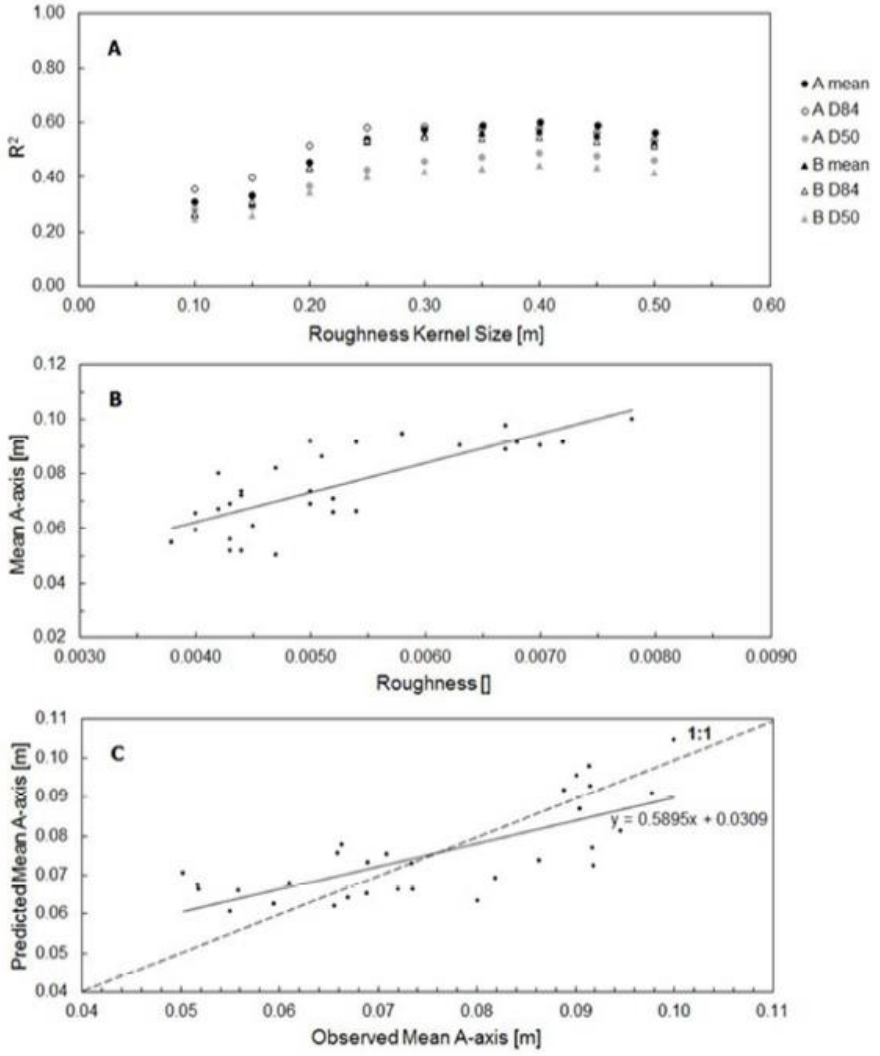

Figure 13. Grain size mapping quality for the P3P using point cloud roughness. A) Calibration model quality. Results for each measure of grain size are plotted against roughness kernel size. B) Best calibration result. C) Best validation result with a mean error of 0.07 mm and a standard deviation of error of 10.15 mm. Maximum error is 19.46 mm.